Journal of
Astronomical Telescopes, Instruments, and Systems

AstronomicalTelescopes.SPIEDigitalLibrary.org

Ion beam planarization of optical aluminum surfaces

Melanie Ulitschka
Jens Bauer
Frank Frost
Thomas Arnold

SPIE.

Melanie Ulitschka, Jens Bauer, Frank Frost, Thomas Arnold, "Ion beam planarization of optical aluminum surfaces," *J. Astron. Telesc. Instrum. Syst.* **6**(1), 014001 (2020), doi: 10.1117/1.JATIS.6.1.014001

Ion beam planarization of optical aluminum surfaces

Melanie Ulitschka,[a,*] Jens Bauer,[a] Frank Frost,[b] and Thomas Arnold[a,b]
[a]Leibniz Institute of Surface Engineering, Leipzig, Germany
[b]Technische Universität Dresden, Institute of Manufacturing Science and Engineering, Dresden, Germany

Abstract. For fabrication of high-performance mirror devices, technical aluminum alloys Al6061 or Al905 are widely used. The surface error topography after manufacturing by single-point diamond turning is applicable in the infrared spectral range. For increasing demands on the optical surface quality in the shortwave visible and ultraviolet spectral range, further improvement of the surface roughness is required. Hence, a promising alternative process to attain the required surface quality is evaluated. Within the ion beam planarization technique, a photoresist layer is deposited by conventional spin coating or spray coating technologies exhibiting an ultrasmooth surface. When removing the resist by reactive ion beam etch (RIBE) processing using nitrogen process gas, the ultrasmooth surface topography of the resist is transferred into the substrate. We optimized the photoresist thermal pretreatment to realize roughness preservation and a steady-state material removal rate during RIBE machining. The optimum preparation steps are explored based on roughness evaluation, chemical modification, and etch resistance of the negative photoresist. Reactive ion beam etching-based planarization is conducted on single-point diamond turned RSA Al905 and RSA Al6061 samples made of rapidly solidified aluminum (RSA) in a two-step process. The optimum process and the roughness evaluation are explored by topographic analysis applying a combination of white light interferometry and atomic force microscopy measurements. © *The Authors. Published by SPIE under a Creative Commons Attribution 4.0 Unported License. Distribution or reproduction of this work in whole or in part requires full attribution of the original publication, including its DOI.* [DOI: 10.1117/1.JATIS.6.1.014001]

Keywords: aluminum; ion beam planarization; reactive ion beam etching; mirrors; ultraprecision machining; smoothing.

Paper 19085 received Aug. 14, 2019; accepted for publication Jan. 2, 2020; published online Jan. 22, 2020.

1 Introduction

Optical mirrors are designed to reflect light for a variety of applications, including beam steering, interferometry, imaging, or illumination.[1–3] An alternative to conventional glass as a substrate material for a metallization layer as a mirror device is aluminum. High-strength and low-weight large-scalable mirror optics can be designed.[4,5] Aluminum is lightweight, cheap, and readily formable with outstanding optical properties. Additionally, aluminum has a high-reflection coefficient even in the shortwave range. The reflection coefficient ranges from the infrared (IR) spectral range to the shortwave visible (VIS) and ultraviolet (UV) spectral range with values well above 90% and, therefore, exceeds optical materials like gold, silver, or copper.[6]

Single-point diamond turning (SPDT) is used to figure metal surfaces in optical fabrication. The optical surface has roughness values of typically below 10 nm root mean square (rms) and at best 2 to 3 nm, regarding the required precision for applications in the near-infrared and IR spectral range.[3,4,7,8] Modern telescope optics for space applications based on three-mirror-anastigmat are designed of ultraprecise aluminum mirrors. The machined surface after SPDT still has the periodic groove pattern microstructures left by the cutting tool. Those so-called turning marks have a pitch of some microns and an amplitude ranging between 10 and 30 nm. As a result, for short-wavelength applications in the VIS and UV spectral range, these periodic patterns have effects similar to that of a diffraction grating.[8,9] To minimize scatter losses by

*Address all correspondence to Melanie Ulitschka, E-mail: melanie.ulitschka@iom-leipzig.de

removing these structures, one technological solution is the electroless plating with an amorphous nickel phosphorous (NiP) layer.[3,8,9]

NiP has an isotropic amorphous matrix that is suitable for the following combination of SPDT and polishing process. Diamond-turned NiP reveals even smoother surfaces than aluminum; it can be further improved by the ion beam planarization (IBP) process, and turning marks are successfully reduced. A further decrease in surface roughness can be obtained by multiple run IBP processing.[10,11] Hence, microroughness values of <1 nm are achievable, resulting in ultraprecise optical surfaces for VIS applications. An additional metallization layer on top of the NiP coating is necessary to realize the desired reflective properties for the specific application.

The mismatch of thermal expansion coefficients between aluminum and NiP coating can cause mechanical stress formation under thermal load conditions, resulting in bending and distortion of the optical surface.[12]

One promising technology for overcoming these drawbacks is reactive ion beam etch (RIBE) processing. In contrast to ion beam figuring (IBF) with an inert gas like argon, where the roughness of the aluminum surface increases rapidly during the process, the operation with reactive process gases such as oxygen and nitrogen allows the preservation of the initial surface topography during ion beam processing.[13,14] Thus this technology allows figure error correction of aluminum mirrors without degradation of the surface quality.

For applications in the short-wavelength VIS or UV spectral range, it is necessary to improve the high-spatial frequency properties of the surface after SPDT. Johnson et al.[15] proposed an ion polishing technique with the aid of a planarizing film to remove polishing scratches on fused silica.[16] As illustrated in Fig. 1(a), the initial surface is covered with a planarizing layer of a specific thickness, so the high-spatial frequency surface roughness features are fully embedded and surface waviness is leveled to a considerable extend. As a result, a smooth and planar surface is revealed. Depending on the initial surface quality, the thickness of the planarizing film typically ranges between some 100 nm and a few microns. Then the plane surface is transferred into the underlying substrate by ion beam etching. To ensure an optimum surface transfer, the etch rates of planarizing film and aluminum substrate should be equal. The ratio of the etch rates

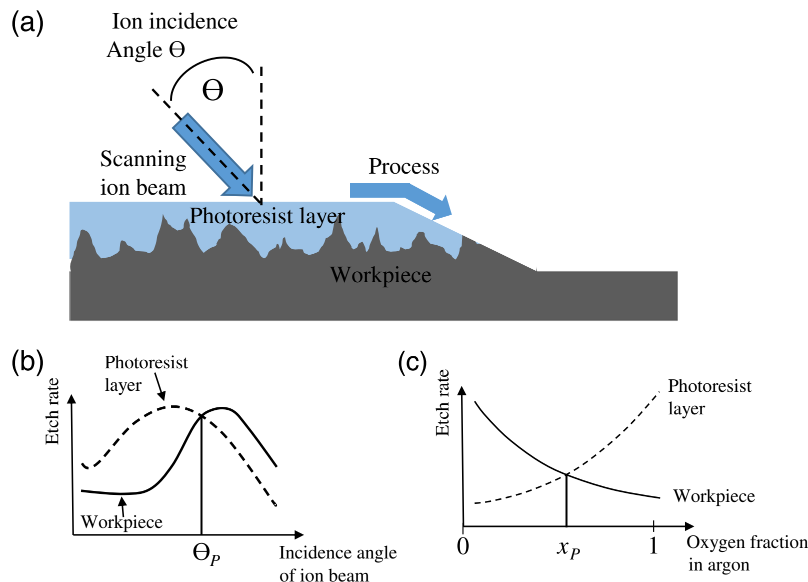

Fig. 1 Principle of (a) IBP technique according to Johnson et al. Illustration of plane surface transfer of planarization layer into aluminum workpiece by scanning ion beam. (b) Dependency of etch rate for workpiece and coating material on incidence angle of ion beam. Planarization angle (θ_P) is marked as point of intersection for both curves. (c) Etch rate dependency of photoresist layer and workpiece on process gas composition and resulting selectivity. An intersection point of both curves (x_P) for a specific operating gas mixture is marked.

between aluminum substrate and planarizing film is defined as the selectivity. Usually, the ion beam etch rates differ for the material to be machined.

Hence, to achieve a successful IBP, the process conditions have to be customized to the specific material combination. In pure physical etching, i.e., ion beam sputtering, the etch rate strongly depends on the ion energy and the ion incidence angle. However, the scaling of the etch rate with respect to the ion energy behaves similarly for most materials. By contrast, the specific characteristics of the ion incidence angle can be considerably diverse for different materials to be machined. So, for many material combinations, there is a crossing in the incidence angle-dependent etch rate characteristics, which is defined by the so-called planarization angle [see Fig. 1(b)]. Thus processing at the planarization angle θ_P is one common solution for realizing equal etch rates for both materials.

If the removal process is dominated by chemical ion-surface-interactions, the etch rate can be additionally adjusted by the process gas composition as well as the ion energy [see Fig. 1(c)]. For many material combinations, there is also a crossing of operating gas mixture-dependent etch rate, which is marked with an intersection point x_P. In ion beam processing with reactive process control, there is a mixture of physically and chemically driven etch removal, so extended degrees of freedom are available for process development.

Polymer coatings are an excellent choice for the IBP technique. A negative photoresist as the planarizing layer has several merits. The resist film can conveniently be applied by industrial standard techniques like spin coating or spray coating, the thickness is controllable by spin speed and dilution, and the cross-linking of the negative working photoresist during exposure to UV light reduces the photosensitivity significantly.

This paper focuses on IBP using a nitrogen-containing process gas at normal ion incidence angle of commercially available rapidly solidified aluminum (RSA) alloys RSA Al905 and RSA Al6061 with the aid of a photoresist layer. For rapid solidification, the melt spinning process is applied. As a result, the polycrystalline material matrix contains grains with a few micrometers in size only. Hence, RSA material is harder than coarse grain aluminum and exhibits an increased stiffness with improved device construction properties. Furthermore, RSA seems very promising for applications in the VIS and UV spectral range due to the reduced surface roughness compared with standard aluminum alloy materials. According to Gubbels et al.[2], RSA Al6061 mainly contains Mg, Si, Cu, Fe, and portions of Cr, Mn, Ti, and Zr within the aluminum base. By contrast, ter Horst et al.[17] found a reduced composition consisting of Mg, Si, and Cu within the aluminum. During RIBE processing with oxygen, significant Si and Mg fractions are found to accumulate together within the etch pits.[13] Consequently, to avoid inhomogeneous matrix structure effects, a so-called "second generation" aluminum alloy RSA Al905 was additionally tested; it does not contain Si and Mg, but mainly Ni, Cu, Fe, and portions of Mn, Zr, and Mo within the aluminum base.[17] In contrast to RSA Al6061, the second alloy material RSA Al905 cannot be heat-treated but is dispersion hardened.[17] RSA Al905 was found to form less etch pits with smaller sizes in the submicrometer range compared with RSA Al6061.[13]

After a description of the experimental setup in Sec. 2, we subsequently report the influence of temperature, deep-UV (DUV) exposure, and RIBE processing on the chemical composition and surface roughness of negative tone photoresist in Secs. 3.1 and 3.2. The influence of RIBE processing on roughness evaluation and chemical composition of RSA Al905 and RSA Al6061 is reported in Sec. 3.3. Finally, the possibilities of IBP with reactive process control are elucidated in Sec. 3.4. The etch behavior is analyzed with a distinct focus on the surface roughness and the local chemical modification.

2 Experimental

2.1 *Sample Preparation*

The negative working photoresist ma-N 2405 (microresist technology) was used as the planarization layer. The photoresist is one type of the ma-N 2400 series. The ma-N 2405 type is specified with a dynamic viscosity of $((8 \pm 1)$ mPa s resulting in approximately (0.5 ± 0.05) μm film thickness during a 30-s spin-coating application at 3000 rotations per

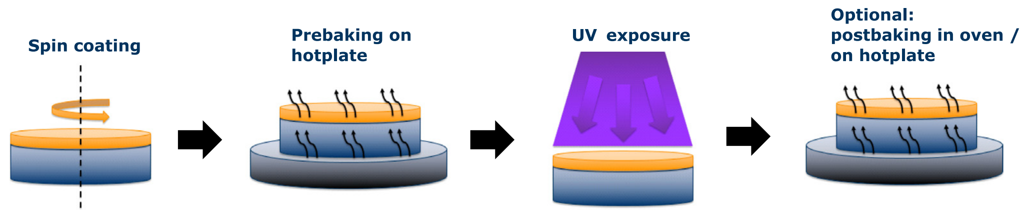

Fig. 2 Illustration of processing steps of a negative tone photoresist application.

minute.[18] Aluminum disc samples were cleaned with acetone and polished p-type Si (100) wafers were cleaned with isopropanol prior to photoresist coating. Conventional UV irradiation in a photolithography system was applied to provide a homogeneous and well cross-linked polymer matrix. The process steps are illustrated in Fig. 2. First, the photoresist is deposited using a spin coater for 30 s at 3000 rotations per minute. In accordance with the thickness of the substrate materials, the baking times for silicon wafer and aluminum substrate were adapted. Since the aluminum disc samples are about 15-mm-thick and silicon wafer are ~0.3-mm thick, longer baking times on the hotplate were chosen for aluminum substrates. Consequently, the resist film is baked on a hotplate in air at 90°C for 2 min on silicon wafer and for 6 min on aluminum.

DUV exposure is performed using a mercury short arc lamp that has an intensity dispersion of 13 and 5 $\mathrm{mW/cm^2}$ for specific wavelengths of 405 and 365 nm, respectively. Due to the small overlap of the lamp emission spectrum and the absorption spectrum of the negative photoresist ma-N 2405, a relatively long exposure time of 120 s was chosen.[18,19] The postbaking step was applied at 150°C on a hotplate for 2 min on silicon wafer and 10 min on aluminum. After all application steps, the photoresist layer thickness was ~500 nm. The optimized preparation parameters for photoresist application are summarized in Table 1.

2.2 *Ion Beam Etching Parameters*

Ion beam machining experiments were performed in a high vacuum chamber with a base pressure of 4×10^{-5} Pa. The ion beam was generated by a 13.56-MHz radio frequency (RF) ion source with a focusing triple grid extraction system allowing a constriction of the free-beam without use of an aperture.[20] The water-cooled sample holder is mounted on a five-axis motion system. The water cooling ensures efficient heat dissipation from the sample, reducing thermal affects during the process.

A Faraday cup is integrated into the sample holder and permits *in situ* spatially resolved beam current density analysis before and after each etching run to determine the ion beam tool function and verify their stability. Usually, the process conditions are chosen to result in a Gaussian shaped tool function and thus can be characterized by the full-width at half-maximum (FWHM) expressing the tool width and the integral beam current. We used nitrogen and oxygen process gas for the generation of low-energy ion beams at $\leq$1.5 kV beam voltage. The FWHM was typically 4 to 15 mm. The RIBE machining experiments were performed at normal ion beam incidence angle to the substrate surface.

Table 1 Photoresist preparation steps depending on substrate material thickness. Prebaking was performed at 90°C and postbaking at 150°C on a hotplate in air. The substrates were heated up to the maximum temperature in conjunction with the hotplate. The samples were cooled to room temperature in air.

Substrate material	Substrate cleaning	Prebaking at 90°C (min)	Postbaking at 150°C (min)
Aluminum RSA 905	Acetone	6	10
Aluminum RSA 6061	Acetone	6	10
Silicon ⟨100⟩	Isopropanol	2	2

Table 2 Ion beam process parameters and corresponding etch rates of aluminum disc samples RSA Al905 and RSA Al6061. The calculated selectivity results from the ratio of the etch rate of aluminum to the etch rate of photoresist layer.

Material/process		Process gas	Process pressure (Pa)	FWHM (mm)	Beam current (mA)	Etch rate (mm^3/h)	Selectivity
Al905 (RSA)		N_2	3.8×10^{-3}	9.9	1.94	0.54	
RIBE planarization	First run	N_2	3.8×10^{-3}	9.8	1.97		0.52
	Second run	N_2	1.6×10^{-3}	8.4	1.89		0.55
RIBE finishing		O_2	1.3×10^{-3}	4.3	1.68		
Al6061 (RSA)		N_2	1.5×10^{-3}	9.0	1.89	0.68	
RIBE planarization	First run	N_2	1.5×10^{-3}	8.6	2.02		0.63
	Second run	N_2	1.7×10^{-3}	9.4	2.14		0.59
RIBE finishing		O_2	1.0×10^{-3}	3.6	1.59		

Preliminary experiments on photoresist layers were performed on spin-coated silicon wafers with a diameter of 2 in. Additionally, the spin-coated silicon wafers were mounted on the water-cooled sample holder with a heat-conducting grease between them to optimize the heat transport. An aluminum mask with an opening diameter of 13 mm defined the machining area for ion beam test etching experiments to determine the etch rates of the planarization layer and aluminum. The ion beam was scanned s-like over the surface with a constant velocity of 4 mm/s and a line pitch of 1 mm. For each repetition, a mask border overrun of the scan area was conducted to ensure a planar etch profile inside the opening area.

IBP experiments on RSA Al6061 and RSA Al905 were performed in a two-step process. In the first planarization process step, the entire aluminum mirror surface, coated with the photoresist layer without an additional mask, was etched with N_2. During this process step, 8 to 10 scan repetitions are necessary to remove the whole photoresist layer. In the subsequent second process step, the whole aluminum surface was etched directly with O_2 operating gas within one scan repetition. The constant velocity of the second process step was chosen at 5 mm/s and 1 mm line pitch. For the second RIBE finishing step, no photoresist layer was used.

The experiments were performed on aluminum planar disc samples with 47-mm in diameter made of RSA Al905 and RSA Al6061 (RSP technology).[21] The ion beam process parameter for IBP processes and direct aluminum machining are summarized in Table 2.

2.3 *Surface Analysis*

The chemical composition of the photoresist was measured by IR spectroscopy using a Bruker IFS 55 armed with a 64 deg grazing angle attenuated total reflection (ATR) accessory (Harrick VariGATR™) with a coupled MCT detector. Thermal gravimetric analysis (TGA) was performed with a Perkin Elmer model Pyris 1 instrument. The measurements were executed in nitrogen atmosphere at a heating rate of 20 K/min in the temperature range of room temperature to 800°C. Differential Scanning Calorimetry (DSC) analysis was performed with a Perkin Elmer model DSC 8500. The measurements were executed in nitrogen atmosphere at a heating rate of 10 K/min. The photoresist thickness was measured using a thin-film analyzing system (Mikropack NanoCalc 2000).

Gas chromatography/mass spectrometry (GC/MS) measurements were performed with a Agilent 5973 series. The measurements were conducted in vacuum at a heating rate of 10 K/min in the temperature range of 45°C to 310°C. Surface composition analysis of the modified layer formed during RIBE was monitored by x-ray photoelectron spectroscopy (XPS, Kratos Ultra DLD). An Al x-ray source with monochromator provides the Al Kα line at 1486.6 eV. Photoelectrons are released from the 300 μm $\times$ 800 μm analysis area. A retarding lens system coupled by a hemispherical analyzer with 40 eV pass energy is used for energy

Table 3 Image sizes and spatial frequency ranges for sample topography measurements by AFM and WLI.

	Image size	Spatial frequency range
AFM	$3\ \mu m \times 3\ \mu m$	1.67 to 34.7 μm^{-1}
AFM	$10\ \mu m \times 10\ \mu m$	0.478 to 19.96 μm^{-1}
AFM	$35\ \mu m \times 35\ \mu m$	0.0857 to 7.31 μm^{-1}
WLI (10× objective)	$624\ \mu m \times 467\ \mu m$	0.00481to 0.120 μm^{-1}
WLI (5× objective)	$1230\ \mu m \times 925\ \mu m$	0.00243 to 0.0786 μm^{-1}

separation. The energy filtered photoelectrons are amplified passing a microchannel plate and recorded with a delay line detector.

The sample topography was analyzed by white light interferometry (WLI; Bruker NPFLEX™ 3D Surface Metrology System) and atomic force microscopy (AFM; Bruker Dimension ICON). For WLI, objectives with 5× and 10× magnifications were used with 1× field-of-view multiplier in phase-shift interferometry mode. The image sizes were $1230\ \mu m \times 925\ \mu m$ and $624\ \mu m \times 467\ \mu m$, respectively, with a pixel resolution of 640×480.

AFM was operated in tapping mode™ in a *xy*-closed loop configuration. Scanning areas of $3\ \mu m \times 3\ \mu m$, $10\ \mu m \times 10\ \mu m$, and $35\ \mu m \times 35\ \mu m$ were measured with a pixel resolution of 1024×1024. The AFM raw data are subjected to a plane correction performed in SPIP™ software (version 6.0.14 by Image Metrology).[22] The correction consists of polynomial fit of the first order and a line-wise correction to subtract a fitted polynomial function of the third order from each scan line.

The surface roughness was analyzed by calculating the power spectral density (PSD) function using the SPIP™ software.[22] A self-written MATLAB® script was employed for angular integration resulting in the isotropic PSD. The spatial wavelength ranges for the different AFM and WLI measurements are summarized in Table 3. The rms roughness values are derived from the composite PSD function, which is a combination of the single measurements PSD functions in the spatial frequency range of 0.0024 to 34.7 μm^{-1}. Waviness and roughness rms values are calculated in the spatial frequency range of 0.0024 to 1.7 μm^{-1}. In the range of 1.7 to 34.7 μm^{-1}, the microroughness rms values are calculated.

Measurements on aluminum and photoresist surfaces were performed five times under the same conditions but at different positions to calculate an averaged PSD function. Since the RIBE planarization process is conducted on the whole substrate surface of 47 mm in diameter, each measurement was performed eight times under the same conditions but at different positions.

Surface composition mapping of aluminum samples is performed by secondary-electron microscope energy dispersive x-ray (SEM-EDX) measurements in a Zeiss Gemini Ultra 55 machine with a Bruker XFlash 3001 detector. A beam voltage of 15 kV, a beam aperture of 60 μm, and a working distance of 7.2 mm are applied.

Depth profiling of the sample composition in the near-surface region was done by dynamic time-of-flight secondary ion mass spectrometry (TOF-SIMS V; IONTOF). Qualitative composition analysis of RSA samples is performed in positive mode. For sputtering, a 1-keV oxygen ion beam is used. The aluminum near-surface region is examined in negative mode, in which a 500-eV caesium ion beam is applied for depth sputtering. The analysis is done by a 15-keV Ga ion beam, whereas the analysis scan field of $(50 \times 50)\ \mu m^2$ is centered within the $(300 \times 300)\ \mu m^2$ sputter crater. The depth calibrations are provided by WLI analysis of the sputter crater depths.

3 Results and Discussion

3.1 *Influence of Preparation Parameters on ma-N 2405 Negative Resist*

The DUV sensitive negative tone photoresist ma-N 2405 is composed of a novolak as polymeric matrix, the biazide as photoactive compound (PAC), and an organic solvent consisting of anisole

and cyclopentanone.[18,23] During exposure, the solubility of negative working photoresist is reduced. The organic solvent is essential for depressing the viscosity of the solution to realize the spray or spin coating onto workpieces.[23,24] The negative photoresist ma-N 2405 is applied by spin coating on the workpiece, prebaking, and exposing in DUV light. The remaining organic solvent is reduced by prebaking and optional postbaking to prevent bubbling by evaporating solvent during subsequent thermal processes and to increase the etch resistance and thermal stability (see Fig. 2).[18] The baking temperatures range from 90°C to 110°C for the prebaking and postbaking steps.[18]

To improve the resistance of the negative photoresist ma-N 2405 for RIBE processing, the applications steps DUV exposure and postbaking are examined in detail in the following. During DUV exposure, the azide groups of the PAC ($R - N_3$) release nitrogen and the resulting reactive nitrenes (R–N:) initiate the cross-linking of the resist.[23,25–27] To ensure a proper cross-linking state by the applied exposure routine, IR spectroscopic measurements were performed before and after DUV exposure of the negative photoresist ma-N 2405. For that reason, the following conclusions about the polymer matrix state are drawn from the relevant vibration mode frequency bands as marked in Fig. 3.

The measured IR spectra of the negative photoresist ma-N 2405 (black curve in Fig. 3) show the characteristic absorptions of a phenolic structure[23,28–31] and of the azide groups ($-N_3$) of the PAC with three main characteristic vibrational bands. The strong frequency in the region of 2160 to 2090 cm^{-1} corresponds to the asymmetric stretching vibration. The symmetric stretching vibration is located at 1340 to 1180 cm^{-1}, and the azide bending vibration is around 700 cm^{-1}.[23,32]

After DUV exposure of ma-N 2405 (blue curve in Fig. 3), the peak intensities in the range of 3600 to 2900 cm^{-1} increase. This may be due to the reaction of the hydroxyl group of the novolak polymer with the intermediate of the photoinduced decomposition of the biazide.[23] Partially reduced peak intensities in the relative broad region of 1720 to 1000 cm^{-1} might result from PAC decomposition since deformation vibrations of $-NH_2$ or –NH or –CN stretching vibrations of the PAC are located in this region.[23,26,28] The peak intensities dedicated to the azide group of the PAC located at 2108 cm^{-1} (asymmetric stretching), 1340 to 1180 cm^{-1} (symmetric stretching) and ~700 cm^{-1} (bending) decrease immensely. This behavior is consistent with the cross-linking mechanism of the negative photoresist.[23,25,27] In correlation with the decomposition of the PAC, the peak intensities decrease; therefore, the probability of cross-linking within the polymer network is increased.

To provide optimum photoresist layers for RIBE processing, the thermal stability limits of the photoresist and the organic solvent were investigated by TGA, GC/MS, and DSC. The results of DSC and TGA measurements of ma-N 2405 resist after DUV exposure, prebaking, and postbaking are in good agreement with results from Ref. 33, who did a careful resin preparation of phenol formaldehyde polycondensates to ensure no entrapped organic solvent. GC/MS measurements of the negative tone photoresist before and after postbaking indicate that remaining amounts of organic solvent (cyclopentanone and anisole) after prebaking are almost completely

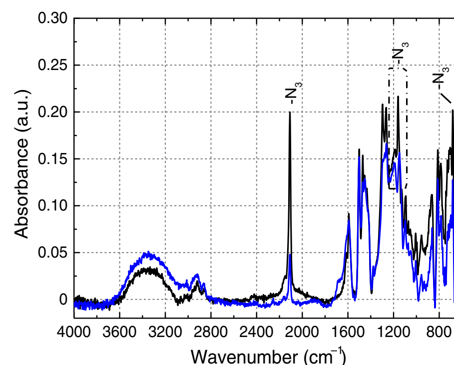

Fig. 3 ATR-IR measurements of negative photoresist ma-N 2405 before DUV exposure (black curve) and after DUV exposure (blue curve). Peak intensities dedicated to azide groups of PAC decrease immensely during DUV exposure.

removed during the subsequent postbaking at 150°C. Postbaking at elevated temperatures above 200°C may avert the beginning of the thermo-oxidative degradation mechanism proposed by Jackson and Conley et al.,[33] Conley,[34] and Shulman and Lochte.[35] The main degradation reaction of the polymer backbone occurs from ∼300°C to 600°C.[33–36]

This result is of major importance since the degradation mechanism can also be expected to appear during ion beam treatments if the heat dissipation is not sufficient. Indeed, a strong resin degradation was observed either at high-ion current densities, which are accompanied by a strong thermal impact into the resist layer, or for insufficient sample cooling.

To obtain reliable, reproducible results, the ion beam experiments were carried out with a water-cooled sample holder. Furthermore, the samples are mounted with the aid of a heat-conducting grease to allow good thermal contact during ion beam processing. To avoid too high-ion current densities, the working distance, i.e., the spacing between ion source and sample, was usually chosen >50 mm.

The influence of photoresist postbaking on surface roughness was investigated by AFM measurements. The negative photoresist ma-N 2405 was spin coated on a silicon wafer, prebaked, and DUV exposed; this is referred to as prepared. The photoresist was postbaked afterward at 150°C, 300°C, and 450°C, respectively. The surface of each sample was measured by AFM [see Fig. 4(a)]. Figure 4(b) illustrates the calculated PSD function based on AFM measurements ($3\ \mu m \times 3\ \mu m$ and $35\ \mu m \times 35\ \mu m$) of the as-prepared surface and subsequently postbaking, respectively. The deviation of the PSD curve after postbake in comparison with the PSD curve of the as prepared surface is an amount of surface degradation with regard to the spatial frequency.

The initial surface roughness of ∼0.35 nm rms is preserved after postbaking at 150°C. In the spatial frequency range below $0.3\ \mu m^{-1}$, the PSD spectrum is even decreased. That may be attributed to a structural reorganization and flowing occurring above the glass transition temperature of noncross-linked areas of the novolak matrix.

For higher temperatures, a degradation is observed. In particular, the roughness is increased to values of 0.45 nm rms after 300°C postbaking temperature and 0.7 nm rms after 450°C postbaking temperature, respectively. As a consequence, the PSD deviation after 300°C is slightly increased and after 450°C is significantly increased over the whole spatial frequency range. The strongest degradation is obtained at 450°C postbaking. In particular, above $3\ \mu m^{-1}$ and below $0.3\ \mu m^{-1}$, the PSD deviation of the 450°C treated sample is strongly increased. These deviations correlate to surface features with sizes below 330 nm and above 3.3 μm, respectively. A maximum deviation of ∼1 decade (dec) is obtained at $0.1\ \mu m^{-1}$. Due to progressive polymer degradation, areas with weaker bonds in the chemical structure of the polymer may preferentially be cracked. Thus the layer thickness decreases irregularly, and consequently surface features of ≥3 μm lateral size are formed.[33,37–39]

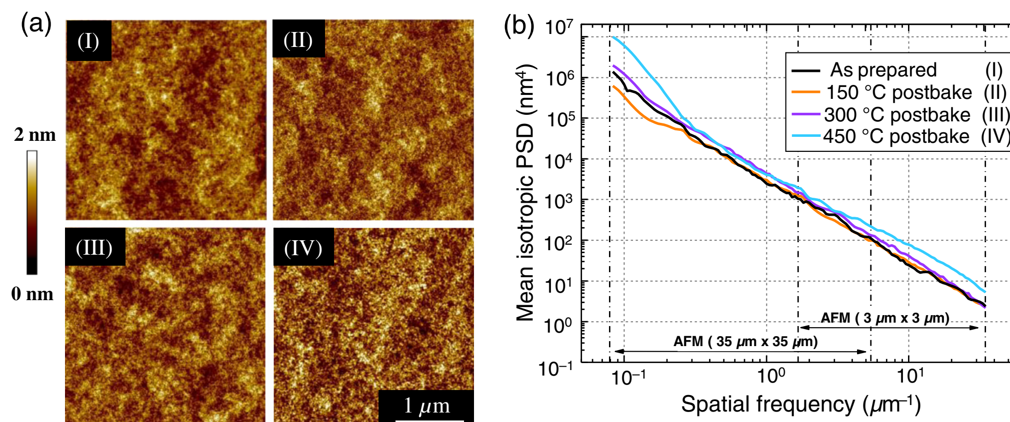

Fig. 4 (a) AFM measurements ($3\ \mu m \times 3\ \mu m$) of negative photoresist ma-N 2405 (I) before and after different postbaking temperatures at (II) 150°C, (III) 300°C, and (IV) 450°C, respectively. (b) PSD function calculated on the basis of AFM measurements with scan sizes of $3\ \mu m \times 3\ \mu m$ and $35\ \mu m \times 35\ \mu m$.

The chosen temperature of 300°C correlates with the beginning of novolak degradation. At that stage, the polymeric backbone is cracked and fragments of different sizes start to evolve. With progressive decomposition, the formation of larger fragments increases. These fragments leave voids in the surface of the photoresist layer of different sizes and may cause the roughness increase in the spatial frequency range above 3 μm^{-1}.[33]

From the results obtained, a postbaking temperature of 150°C has been identified to be optimal. The postbaking temperature for subsequent experiments is determined at 150°C since the initial surface roughness is preserved and no novolak degradation occurs. In addition no structural changes of the novolak matrix are observed. Similar results were investigated by Voigt.[23]

For IBP, postbaking of the photoresist layer is an important processing step to ensure roughness preservation. For preliminary experiments, photoresist was applied on smooth silicon wafers. By contrast, diamond turned aluminum samples RSA Al905 and RSA Al6061 reveal surfaces with periodical turning structures.

To analyze if these periodic features are embedded in spite of the temperature treatment of the 560-nm thin layer, the photoresist was analyzed by AFM measurements before and after postbaking. During postbaking, the photoresist thickness was decreased to about 500 nm. Figure 5 shows AFM measurements and PSD functions of the initial aluminum surface and coated with negative photoresist ma-N 2405 before and after postbaking, respectively.

The initial surface of RSA Al905 is dominated by 3 μm spaced turning marks corresponding to the PSD deviation at 0.3 μm^{-1} with superstructures at 0.7, 1, and 1.4 μm^{-1} [Figs. 5(a) and 5(d)]. After photoresist application, the turning structures were almost fully embedded and a smooth surface is revealed [Fig. 5(b)]. As a consequence, the PSD curve is strongly decreased in the spatial frequency range of 0.086 to 34.7 μm^{-1} and the PSD deviations corresponding to the turning marks are almost completely removed [Fig. 5(d)].

By contrast, these structures become more apparent if postbaking is applied [Fig. 5(c)]. Due to a shrinkage of the thin layer during temperature treatment, the turning marks are transferred into the negative photoresist. On the other hand, the granular structure after exposure is smoothed during heating [see Figs. 5(b) and 5(c)]. This may be attributed to flowing of the polymer due to structural reorganization already observed in Sec. 3.1.[39]

3.2 *Reactive Ion Beam Etching of Negative Photoresist ma-N 2405 Thin Films*

The effect of ion beam irradiation on the resist layer is investigated with a special focus on the surface evolution and the temporal stability of the removal process. For that reason, the process

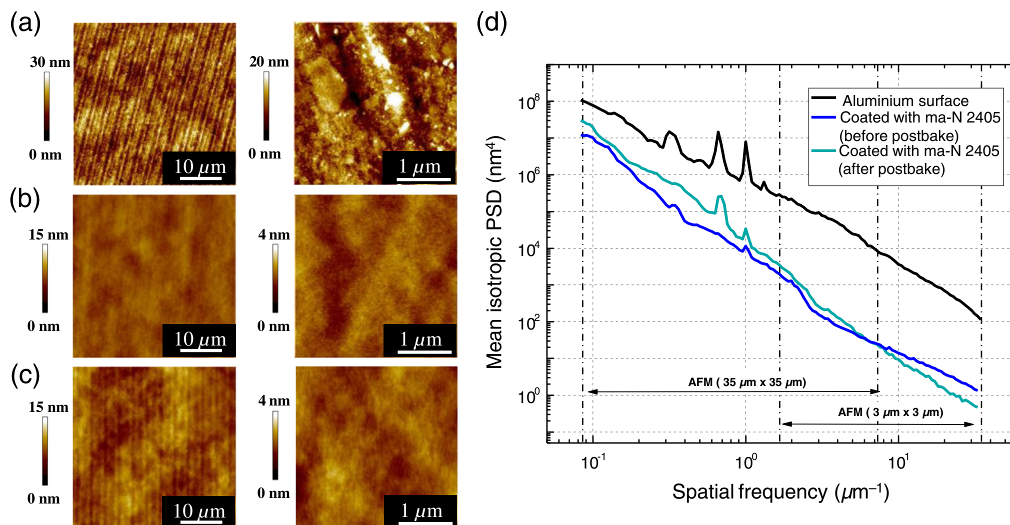

Fig. 5 AFM measurements (3 $\mu m \times 3$ μm and 35 $\mu m \times 35$ μm) of (a) RSA Al905 sample surface, (b) additionally spin-coated with negative photoresist ma-N 2405, prebaked, and DUV exposed, and (c) after subsequent postbaking at 150°C for 10 min. (d) PSD function calculated on the basis of AFM measurements with scan sizes of 3 $\mu m \times 3$ μm and 35 $\mu m \times 35$ μm.

time is stepwise increased. After each step, the surface roughness and the etch rate are examined with respect to the increasing material removal. The ion beam etching experiments on ma-N 2405 are performed under equal ion beam process conditions with N_2 operating gas on aluminum samples as summarized in Table 2.

Figure 6(a) shows AFM measurements of the photoresist layer at various etching depths. The material removal, measured by optical thin film reflectometry, is defined as the difference between the layer thickness before and after RIBE processing. To investigate the effect of the ion beam machining on the surface roughness of the photoresist, the PSD function in the spatial frequency range of 0.086 to 34.7 μm^{-1} is calculated [see Fig. 6(b)].

After 76-nm material removal, the formation of particles and a granular structure with a few nanometers in diameter is observed [see Fig. 6(a)]. As a consequence, the PSD spectrum above 8 μm^{-1} spatial frequency is increased [see Fig. 6(b)]. The PSD deviation increases with increasing etching depth. A contrary effect is observed in the spatial frequency range of 0.9 to 8 μm^{-1}. With increasing material removal, the PSD curve is decreased. The differences in height of the initial surface are perpetually flattened [see Fig. 6(a)]. Between 0.5 and 0.9 μm^{-1}, the PSD curves merge. At spatial frequencies below 0.5 μm^{-1}, the spectrum after 76 nm removal decreases strongly and increases slightly again with further increasing material removal but remains consistently below the initial value [see Fig. 6(b)]. The full range roughness calculated in the spatial frequency range of 0.086 to 34.7 μm^{-1} is mainly preserved during RIBE machining up to 450 nm depth [see Fig. 6(b) inset].

This effect has also been observed in reactive ion etching (RIE) experiments using CHF_3 processing gas performed by Schuster et al.[39] The AFM images after RIE machining with CHF_3 process gas exhibit a similar granular structure. Simultaneously, a smoothing over the whole measured area of 3 $\mu m \times 3$ μm is observed.

For further analysis, XPS measurements are performed on the untreated photoresist layer and after 76 nm material removal as depicted in Fig. 6. During RIBE machining, the top layer of photoresist surface is highly modified. According to the results obtained from XPS measurements, CN_x groups are formed and concurrently CO_x groups are remarkably reduced. In addition, carbon single bonds are partially reorganized to graphitized carbon.

Referring to Sumiya et al.,[37] the schematic of a two-stage photoresist degradation mechanism is consistent with our observations. A certain roughness is initially introduced and constantly transferred into the underlying material during subsequent etching [see Fig. 6(a)]. In the first stage, a modified layer is formed on top of the photoresist surface. During that period, selective oxygen removal occurs and a graphitic layer is formed. The character of the roughness develops during this time period. The increase in microroughness above 8 μm^{-1} spatial frequency observed in the PSD function after 76 nm material removal may originate from this degradation

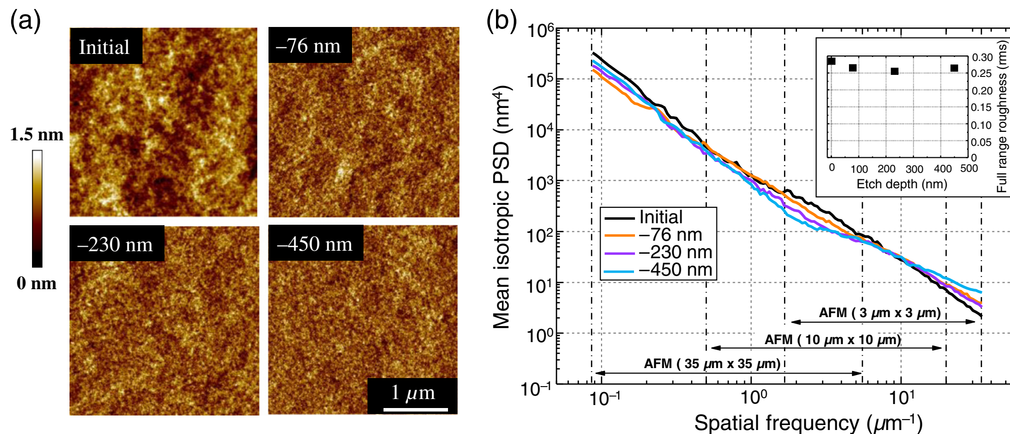

Fig. 6 (a) AFM measurements (3 $\mu m \times 3$ μm) of negative photoresist ma-N 2405 before and after RIBE (N_2 operating gas, 1.2 keV) with machining depths of 76, 230, and 450 nm. (b) PSD functions calculated on the basis of the AFM measurements with scan sizes of 3 $\mu m \times 3$ μm, 10 $\mu m \times 10$ μm, and 35 $\mu m \times 35$ μm. The inlet represents the mainly constant full range roughness dependent on different etch depths.

mechanism. In the second period, a steady-state etching takes place where the spatial distribution of the surface roughness changes little.

The volume etch rate R of the photoresist layer after nitrogen processing at various etch depths d depicted in Fig. 6 is calculated in consideration of the deterministic scan parameters as line velocity v_y, line feed Δx, and scan repetition count N_{rep}

$$R = \frac{d \cdot v_y \cdot \Delta x}{N_{\text{rep}}}. \tag{1}$$

The results are illustrated in Fig. 7 (black curve). The averaged volume etch rate of ma-N 2405 after postbaking at 150°C is 1.10 mm^3/h. As an alternative to the usage of postbaking but also with improved surface qualities after ion irradiation, an increased prebaking time of 5 min at 90°C and subsequent DUV exposure can be applied.

The orange curve in Fig. 7 depicts the ion beam etch rates of photoresist layers prepared in this way. However, the missing postbake results in an increased etch depth of 90 nm and, therefore, a higher etch rate of 1.3 mm^3/h conducted under equal ion beam process conditions. With increasing machining depth up to 300 nm, the etch rate approaches similar steady-state conditions. The different depth-dependent etching behaviors may be due to remaining organic solvent in the thin photoresist layer.

According to Brinke et al.,[40] solvent molecules can act as plasticizers, lowering the glass transition temperature, and thermal flow temperature of the resist film. The higher amount of organic solvent in the partially cross-linked negative photoresist enables polymer chain motion and thermoplastic flow. With increasing material removal, the remaining organic solvent evolves, resulting in the same steady-state etching conditions as the postbaked layer.

Controllable process parameters during the planarization process require no entrapped organic solvent since the volume etch rate of the negative photoresist after postbaking at 150°C for 2 min is nearly constant for all etching depths up to 450 nm. Furthermore, the etch rate is independent of the atmosphere of the postbaking conditions. The experiments are repeated on a photoresist layer postbaked in a vacuum oven at 150°C for 2 min and reveal similar results.

Our results conclude that sufficient pretreatment of the negative photoresist ma-N 2405 including exposure in DUV and heating prevents the polymer from degradation and, therefore, avoids an increase in roughness during ion beam irradiation. Since postbaking at temperatures above 150°C has no improvement on surface roughness or etching resistance, it is not necessary to use elevated temperatures. Furthermore, the resist thickness decreases rapidly with increasing postbaking temperature, and photoresist degradation occurs. Additionally, based on TG/MS and TGA measurements, the remaining organic solvent is removed during postbaking at 150°C. Surface roughness after postbaking at 150°C is preserved during ion beam irradiation with nitrogen process gas. Another advantage is the nearly constant etch rate of different machining depths from 76 up to 450 nm (see Fig. 7) independent of the atmosphere of postbaking. In the following, the photoresist preparation includes spin coating, prebaking at 90°C, DUV exposure, and

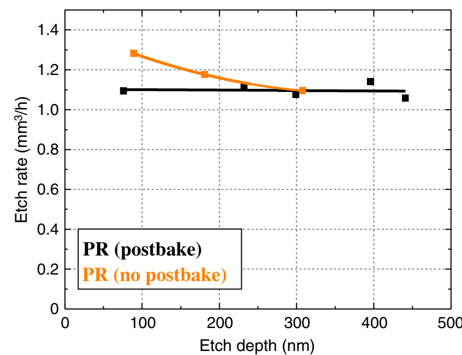

Fig. 7 RIBE volume etch rate of negative photoresist ma-N 2405 depending on etching depths. For comparison, two variations in photoresist processing are focused: photoresist postbaking at 150°C for 2 min (black) and without postbaking but longer prebake at 90°C for 5 min (orange).

postbaking at 150°C unless specified otherwise. Hereby prepared photoresist layers are referred to as initial photoresist surface.

3.3 *Effect of Reactive Ion Beam Etching on Optical RSA Al905 and RSA Al6061 Surfaces*

Direct RIBE machining is performed on both aluminum substrate materials with a special focus on roughness evolution and local composition distribution during the etching process. Additionally, the respective etch rates are calculated to determine the ratio of the etch rates of aluminum substrate and photoresist layer, defined as selectivity. The ion beam process parameter and corresponding etch rates of aluminum disc samples RSA Al905 and RSA Al6061 are summarized in Table 2. Since the etch rate of ma-N 2405 is nearly constant and surface roughness is preserved during RIBE up to 450 nm etching depths, preconditions for IBP are encouraging. To investigate the capability of planarization process on aluminum surfaces, the following approach is chosen. First, the surface roughness of untreated RSA Al6061 and RSA Al905 is determined by AFM and WLI measurements. Direct aluminum machining experiments on both aluminum alloys are performed to calculate the volume etch rate and consequently the selectivity. The RIBE process parameters are summarized in Table 2. The effect of ion beam irradiation on aluminum is investigated with a focus on roughness evolution. Finally, IBP at normal ion incidence angle on RSA Al905 and RSA Al6061 with the aid of ma-N 2405 is investigated with a spatial focus on roughness evolution and local composition distribution after RIBE machining.

Rapid solidified aluminum RSA Al6061 alloy with a smaller grain size compared with conventional Al6061 alloys as well as RSA Al905 is tested. Figure 8 shows AFM topography images and the calculated PSD function of RSA Al905 and RSA Al6061 samples before and after RIBE processing. For a more detailed discussion, the surface roughness is segmented into waviness/roughness and microroughness applying a cut-off frequency of 1.7 μm^{-1}. The corresponding spatial wavelength ranges are marked in Fig. 8(b).

The surface topography of RSA Al905 is generally dominated by 2.4 μm spaced turning marks with an initial height of (23.3 ± 1.9) nm caused by SPDT corresponding to the strong deviation in the PSD spectra at 0.4 μm^{-1} with several superstructures at 0.8, 1.2, 1.6, 2.0, and 2.4 μm^{-1} [Fig. 8(b)]. These superstructures present in the PSD spectra result from multiple-peak structure of the turning marks on the untreated aluminum surface, which might indicate an imperfection in the cutting tool shape. Additionally, a bump in the PSD spectra at about 0.006 μm^{-1} corresponds to 167 μm spaced periodicity results from chatter, i.e., mechanical vibrations of the SPDT machine.

During machining, the PSD curve is increased in the short-wavelength range above 2.6 μm^{-1}. Surface bumps and pits are formed, resulting in a slightly increased microroughness of (4.2 ± 0.5) nm rms compared with (3.8 ± 1.2) nm rms before RIBE machining [Fig. 8(a)]. Below 1.5 μm^{-1}, the PSD deviation after RIBE is almost negligible. The calculated roughness of (9.9 ± 2.3) nm rms in the spatial frequency range of 0.0024 to 34.6 μm^{-1} is largely preserved during processing.

The roughness preservation during RIBE machining of RSA Al905 is convenient for the planarization process since direct aluminum etching takes place after photoresist removal within the interface of planarization layer and aluminum. The turning marks are slightly reduced in height to (16.3 ± 1.3) nm but the formation of etch pits with sizes in the submicrometer range is observed [Fig. 8(a)].

The surface of RSA Al6061 is also characterized by periodic pattern marks caused by SPDT with corresponding PSD deviations (see Fig. 8). Dominant are $\sim$1.3 μm spaced turning marks with a few nanometer in depth. A further periodicity corresponding to 17 μm spatial wavelength is found in the PSD function, which is a result of machine vibrations during SPDT.

By contrast, ion beam irradiation of RSA Al6061 causes surface degradation. Consequently, the PSD spectrum is significantly increased in the spatial frequency range of above 0.15 μm^{-1}. Below 0.15 μm^{-1}, both PSD curves merge [see Fig. 8(b)].

The microroughness is increased to (3.4 ± 1.0) nm rms after machining compared with the initial value of (1.3 ± 0.6) nm rms. The largest deviation of $\sim$1 to 1.5 orders of magnitude is

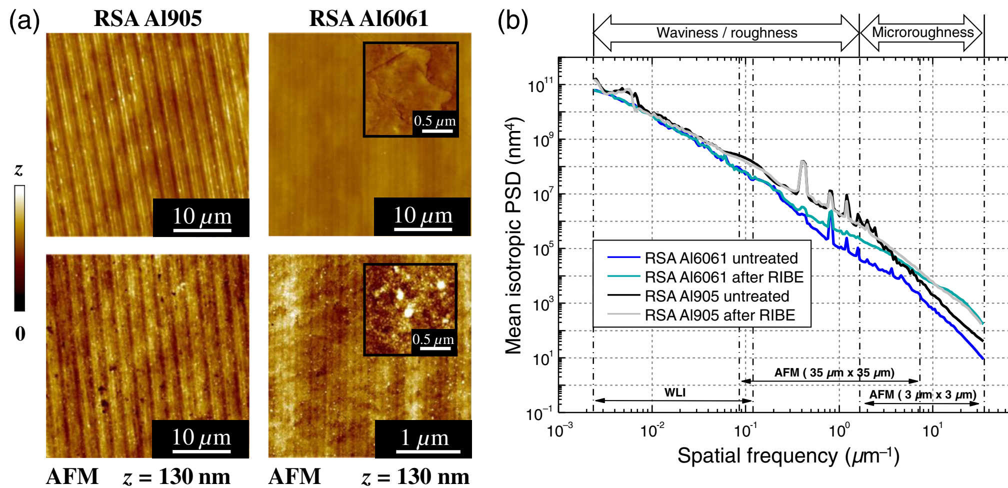

Fig. 8 (a) AFM measurements of RSA Al905 and RSA Al6061 (35 μm $\times$ 35 μm) samples before (top) and after (bottom) RIBE machining with nitrogen process gas at normal angle. The etching depths for both process runs were 300 nm for RSA Al905 and 230 nm for RSA Al6061. The inlets in AFM measurements of RSA Al6061 show the roughness evolution of surface topography on 1.5 μm $\times$ 1.5 μm scan size. The z range of the inlets is 20 nm. (b) PSD function calculated on the basis of AFM measurements with scan sizes of 3 μm $\times$ 3 μm and 35 μm $\times$ 35 μm and WLI measurements with image sizes of 1230 μm $\times$ 925 μm and 624 μm $\times$ 467 μm.

obtained in the high-frequency range above 10 μm^{-1}, which is a result of the formation of a granular structure with sizes below 100 nm.

In the range between 1 and 10 μm^{-1}, there is a deviation in the order of 0.5 to 1 dec resulting from pit and particle formation with individual sizes of several hundred nanometers. As a consequence, the waviness/roughness increases to (5.0 ± 0.6) nm rms compared with the initial value of (4.7 ± 0.8) nm rms. The turning marks are still apparent with smoothed edges but comparable depth. The calculated full range roughness of the untreated RSA Al6061 sample has a value of (4.9 ± 0.9) nm rms and is increased to (6.1 ± 1.1) nm rms after machining.

According to our recent study,[13] no roughening is obtained during RIBE machining using the oxygen process gas of aluminum alloys RSA Al905; the represented results also obtain a preservation of initial surface roughness during RIBE processing with nitrogen process gas.

To further analyze the effect of RSA Al6061 surface degradation, the local composition distribution after RIBE machining is monitored by SEM-EDX mapping (see Fig. 9).

TOF-SIMS experiments performed in positive mode reveal the following constituents beyond the surface region: The used RSA Al6061 alloy contains Mg, Fe, Mn, Cr, Si, Ti, Cu, Ni, and Zr portions in the Al base material. The particles formed on the surface of the RSA Al6061 sample after RIBE machining are mainly due to chromium and silicon fractions. Significant silicon and magnesia fractions are found together within the etch pits. Iron and titanium fractions are also detected on the surface. The surface degradation of RSA Al6061 after RIBE machining with oxygen show similar results as previously reported.[13] Due to the inhomogeneous matrix structure of RSA Al6061 alloy, the formation of pits is promoted, resulting from preferential sputter erosion.

3.4 *Ion Beam Planarization of Optical Aluminum Surfaces*

In this section, IBP and RIBE finishing of optical RSA Al905 and RSA Al6061 aluminum surfaces is described. Preparation parameters of photoresist layers as described in Sec. 3.1 are applied. Surface topography evolution during processing is discussed with special regard to turning mark structure reduction. Ion beam process parameters summarized in Table 2 are also executed for the following IBP experiments.

Hereafter, IBP of RSA Al905 and RSA Al6061 are elucidated. The maximum etch depth was chosen with respect to the initial photoresist thickness of about 500 nm and the height of the

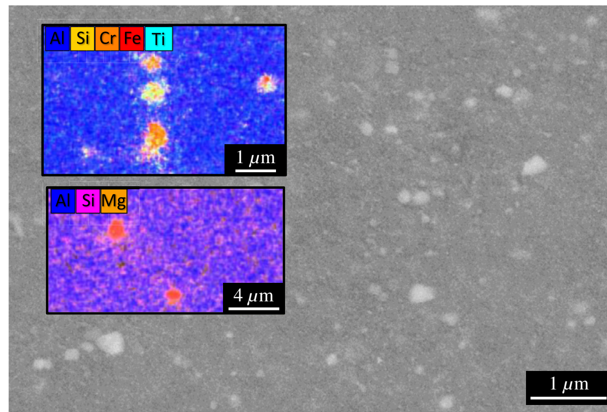

Fig. 9 SEM and SEM-EDX mapping image of a nitrogen processed aluminum RSA Al6061 sample after 300-nm etch depth revealing mainly Si and Mg precipitates within the etch pits.

turning mark structures. Hence, a maximum aluminum removal of 50 nm was not exceeded during processing. The ion beam process parameter for the following IBP and RIBE finishing experiments are summarized in Table 2. For a more detailed discussion of turning mark evolution, averaged cross section profiles are generated by defining an average area for the cross section line. Within this area, about 300 parallel cross sections will be averaged using SPIP™ software.[22]

3.4.1 *Ion beam planarization of optical RSA Al905 surfaces*

Hereafter, the untreated diamond turned aluminum alloy is referred to as untreated surface and the surfaces after the first and second IBP process are referred to as first run and second run, respectively. The topography measurements in Fig. 10(a) represent the RSA Al905 initial aluminum surface.

Figures 10(b) and 10(c) represent the surfaces after first run and second run IBP process, respectively. For more detailed discussion, the PSD distribution of the initial surface and after the first and second runs on the basis of AFM and WLI measurements is calculated [see Fig. 11(a)]. The dashed lines in the AFM images represent the positions for the midlines of the cross sections profiles illustrated in Fig. 11(b).

Before RIBE machining, the surface is dominated by a periodic waviness pattern caused by the SPDT tool, including turning marks with a height of (23.6 ± 0.8) nm on average and mid-spatial frequency errors with a spatial wavelength of $\sim$220 μm [see Fig. 10(a), WLI image]. By way of illustration, in the following conclusions about the roughness evolution during IBP, relevant turning mark spaces and etch pit surface density are marked in Fig. 10.

Although the mid-spatial frequency errors are not fully embedded by the thin photoresist layer, a distinct improvement of these surface errors during IBP is barely to be expected. Hence, the 220-μm spaced surface errors are slightly smoothed during processing but remain almost unchanged [see Figs. 10(a)–10(c), WLI images]. As a result, the bump in the PSD spectrum in the spatial frequency range of 0.0024 to 0.007 μm^{-1} is barely reduced after one planarization run [Fig. 11(a)]. The deviation after the second planarization run is negligible.

The turning marks located in the high-spatial frequency range are characterized by a period of 3 μm with several superstructures of 1.4, 1, and 0.7 μm. These turning marks are considerably reduced in height to an average height of (7.9 ± 0.7) nm with smoothed edges after the first run. As a consequence, the strong deviations in the spatial frequency range of 5 to 0.5 μm^{-1} with several maxima at 0.3, 0.7, 1, and 1.4 μm^{-1} are significantly decreased [see Fig. 11(a)].

The PSD deviation at 1.4 μm^{-1} reflecting one superstructure is almost completely removed. Additionally, the formation of single-etch pits with sizes of a few hundred nanometer and particles with a mean diameter of 90 nm is observed [see Fig. 10(b)]. The turning marks are further reduced to an averaged height of (4.2 ± 0.5) nm after the second run but the formation of etch pits is increased with slightly enhanced diameters in the submicrometer range [see Fig. 10(c)].

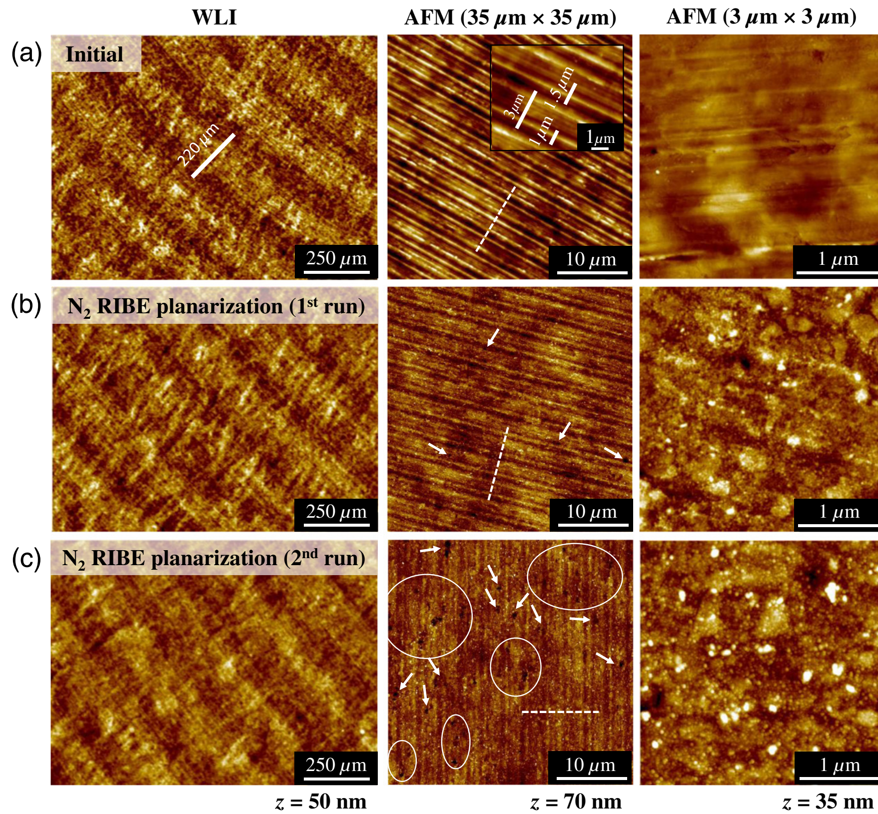

Fig. 10 WLI (5× objective) and AFM (3 μm × 3 μm and 35 μm × 35 μm) measurements of surface topography of RSA Al905 sample of the (a) initial surface and after (b) the first run and (c) second run RIBE planarization. The image height scale is indicated by the z value.

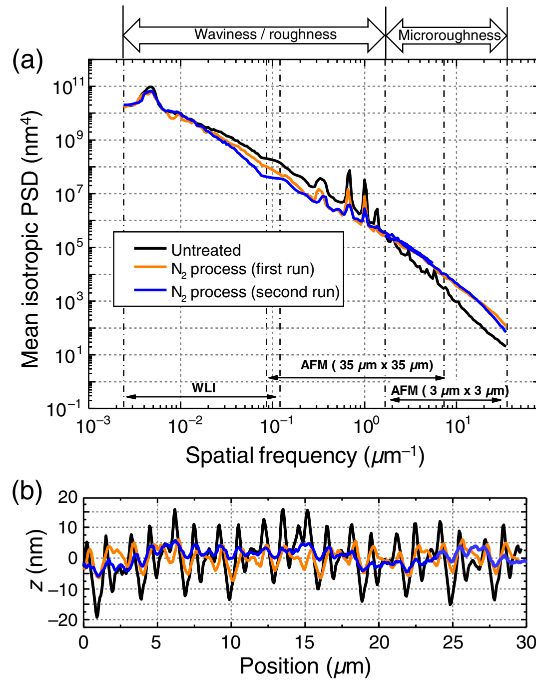

Fig. 11 (a) PSD spectra before and after two planarization runs on RSA Al905 sample. (b) Averaged cross section profiles of aluminum RSA Al905 sample calculated based on AFM images of the untreated surface (black), after the first run (orange) and the second run (blue).

For a more detailed analysis of the roughness evolution with a special focus on the 3-μm spaced turning marks, cross section profiles of the RSA Al905 sample depicted in Fig. 10 are investigated. Fig. 11(b) shows an averaged cross section profile of the untreated surface and after the first and second run, respectively. During the first run, the turning marks are reduced in height by about 66.5% with smoothed edges.

Due to a selectivity of 0.52 of the first planarization run, the height reduction is indeed larger than expected. The reduction of the turning mark height may additionally be enhanced by the ion incidence angle dependent sputter yield as a function of the local surface error slope. Turning marks with high slope border areas result in locally different incidence angles of the incoming ions. Due to the angle dependence of the sputter yield, sputter erosion increases with an increasing angle of incidence to a specific maximum. Consequently, the roughness features with high slope border areas may be gradually smoothed.[41–46]

During the second run, a further reduction of 44.5% in turning mark height is observed, correlating to a selectivity of 0.55. After the second run, the waviness/roughness value is slightly reduced compared with the first run. The turning marks are further reduced in height, leading to a roughness reduction. Counteracting etch pit formation and an increased formation of statistically distributed particles on the surface [see Fig. 10(c)] may lead to the reduced roughness value. The effect of the planarization process on RSA Al905 surface roughness segmented into waviness and microroughness in detail is summarized in Table 4, and the corresponding spatial wavelength ranges are marked in the PSD function in Fig. 11(a).

As a summary of the planarization behavior of RSA Al905 surfaces by RIBE with 1.2 keV nitrogen ions, the turning marks are successfully reduced by 82% overall after two planarization runs. By contrast, the microroughness is increased after the first run with roughness values of ∼2.2 nm rms for the initial surface to 3.2 nm rms after the first run and 3.3 nm rms after the second run [see Figs. 10(a)–10(c)]. As a consequence, the PSD spectrum is increased in the spatial frequency range above 1.6 μm^{-1}. A maximum deviation of about 1 dec is obtained, correlating to a formation of a granular structure with several distributed particles. The microroughness remains unchanged after the second run compared with the first run [see Figs. 10 and 11(a)].

For further analysis of the particulates that are observed on RSA Al905 after the IBP process, the local composition distribution after RIBE machining was monitored by SEM-EDX mapping (see Fig. 12).

Table 4 Surface roughness values of aluminum RSA Al905 and RSA Al6061 divided into waviness/roughness and microroughness corresponding to the spatial frequency range of 0.0024 to 1.7 μm^{-1} and 1.7 to 34.7 μm^{-1}, respectively, and the full range roughness.

		Microroughness (nm rms)	Roughness + waviness (nm rms)	Full range (nm rms)	Turning mark height (nm)
RSA Al905					
Untreated		2.2 ± 1.2	9.5 ± 1.4	9.7 ± 1.6	23.6 ± 0.8
RIBE planarization	First run N_2	3.2 ± 0.3	5.9 ± 0.7	6.8 ± 0.8	7.9 ± 1.3
	Second run N_2	3.3 ± 0.3	5.1 ± 1.1	5.9 ± 1.1	4.3 ± 0.5
RIBE finishing	O_2	2.2 ± 0.6	5.2 ± 0.9	5.7 ± 1.1	6.6 ± 0.6
RSA Al6061					
Untreated		1.3 ± 0.6	4.7 ± 0.8	4.9 ± 0.9	2.9 ± 0.3
RIBE planarization	First run N_2	2.6 ± 0.2	4.2 ± 0.6	4.9 ± 0.7	1.8 ± 0.3
	Second run N_2	2.5 ± 0.3	3.2 ± 0.6	4.0 ± 0.7	<1
RIBE finishing	O_2	1.4 ± 0.2	3.3 ± 0.5	3.6 ± 0.6	<1

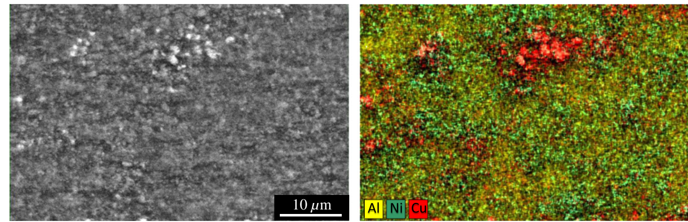

Fig. 12 SEM and SEM-EDX mapping image of an aluminum RSA Al905 alloy after the first run of IBP revealing significant Cu and Ni precipitations.

TOF-SIMS measurements performed in positive mode reveal that the RSA Al905 alloy material mainly contains Ti, Ni, Cu, Ga, Fe, Mn, and Mg and portions of Cd, Mo, Zn, Zr, Cr, and Si in the aluminum base. After the first processing run, Cu and Ni precipitates, in particular, can be observed irregularly distributed over the aluminum surface. The particle formation is assumed to result from the reduced sputter erosion of these precipitates compared with aluminum.

3.4.2 *Ion beam planarization of optical RSA Al6061 surfaces*

The same process is also applied on RSA Al6061. The surface topography measurements in Fig. 13(a) represent the untreated RSA Al6061 sample. Figures 13(b) and 13(c) represent the surface after the first and second planarization runs, respectively. The PSD function distribution of the initial surface and after each planarization run is represented in Fig. 14(a). The positions for the midlines of the cross section profiles illustrated in Fig. 14(b) are represented by dashed lines in the AFM images in Fig. 13.

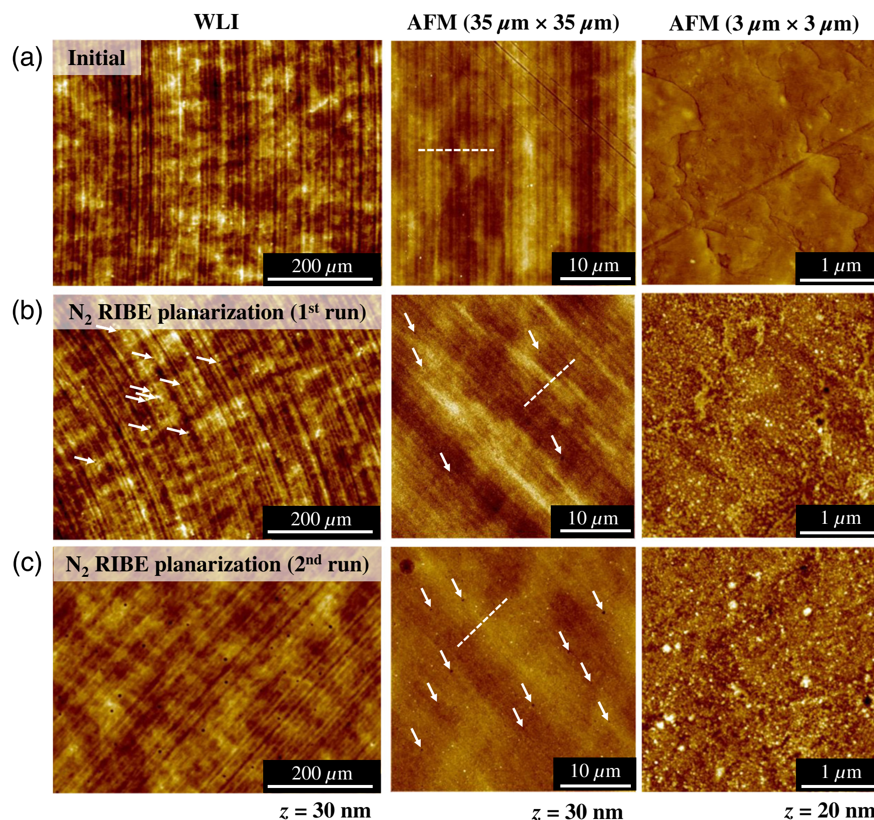

Fig. 13 WLI (10× objective) and AFM (3 μm × 3 μm and 35 μm × 35 μm) measurements of RSA Al6061 sample (a) before and (b) after the first run and (c) second run RIBE planarization. The image height scale is indicated by the z value.

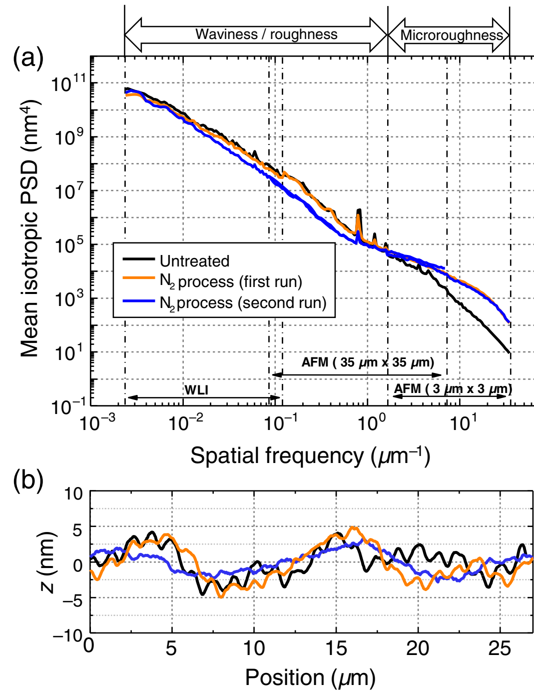

Fig. 14 (a) PSD spectra before and after both RIBE planarization runs on RSA Al6061 sample. (b) Averaged cross section profiles of aluminum RSA Al6061 sample calculated on the basis of AFM images of the untreated surface (black), after the first run (orange) and the second run (blue).

The untreated surface is dominated by $\sim$1.3 μm spaced turning marks with only a few nanometer in depth corresponding to the PSD deviations with maxima at 0.8, 1.2, and 1.6 μm^{-1}. Furthermore, larger spaced turning marks with several nanometers in height correlate to the PSD deviations in the spatial frequency range of $\sim$0.03 to 0.1 μm^{-1}. The initial aluminum surface is dominated by turning marks with an average height of (2.9 ± 0.3) nm.

After the first planarization run, the formation of a few etch pits concentrated within the turning marks with diameter of a few micrometer is observed. After the second run, the etch pit formation is increased with similar mean diameter [see Figs. 13(b) and 13(c)].

The turning marks are reduced in height to an averaged value of (1.8 ± 0.3) nm after the first run. As a consequence, the corresponding PSD deviations in the spatial frequency range of 0.7 to 1.8 μm^{-1} are decreased [Fig. 14(a)]. The full range roughness of (4.9 ± 0.9) nm rms remains unchanged after the first planarization run. This is due to the reduction of the waviness to (4.2 ± 0.6) nm rms and a contrary increase in microroughness to (2.6 ± 0.2) nm rms.

After the second planarization run, the turning marks are strongly reduced to height values in the subnanometer range. Hence, the PSD deviation at 0.8 μm^{-1} is remarkably decreased [see Fig. 14(a)]. Additionally, the PSD deviations at 1.2 and 1.6 μm^{-1} almost disappeared after the second planarization run. The PSD spectrum in the spatial frequency range of 0.01 to 1.6 μm^{-1} decreases. As a consequence, the waviness is remarkably reduced to (3.2 ± 0.6) nm. Figure 14(b) shows an averaged cross section profile of the untreated surface and after the first and second runs, respectively. The 1.25-μm spaced turning marks with (2.9 ± 0.3) nm height on RSA Al6061 are almost completely removed after two planarization runs.

A maximum deviation of about 1 dec is obtained in the spatial frequency range above 10 μm^{-1} correlating to the formation of a granular structure [see Figs. 13 and 14(a)]. The same effect has been observed after the planarization process of RSA Al905 with nitrogen process gas. The grain structure of RSA Al6061 represented in AFM measurements with the small scan size of 3 $\mu m \times 3$ μm is still apparent after the second planarization run. The small particles seem to accumulate together at the grain boundaries. The particles formed after the second run are increased in size and some consist of smaller particles clumped together, resulting in several hundred nanometer size. The effect of the planarization process on RSA Al6061 surface

roughness segmented into waviness/roughness and microroughness in detail is summarized in Table 4 and the corresponding spatial wavelength ranges are marked in the PSD function in Fig. 14(a).

As a summary of the planarization behavior of RSA Al6061 surfaces by RIBE with 1.2 keV nitrogen ions, the turning marks are also successfully reduced in a comparable ratio as already observed during IBP of RSA Al905. However, the turning marks present on the untreated RSA Al6061 surface were already smaller in height. Consequently, these structures are almost completely removed during processing. In consideration of the different surface qualities of the aluminum samples used for IBP investigations, comparable results were obtained.

3.4.3 *RIBE finishing of optical aluminum surfaces after planarization*

After N_2 planarization, the reflectivity of both aluminum surfaces is reduced. The initial aluminum surface exhibiting a native oxide layer shows a high reflectivity over a broad spatial wavelength range. Additionally, the microroughness of both aluminum materials is increased after nitrogen machining and a granular structure with similar particle sizes is formed. As a result of this microroughness, the surface exhibits a diffusive shine. For applications in the VIS and UV spectral range, a further reduction of the increased microroughness is a prerequisite. Thus a subsequent ion beam machining with 1.5 keV oxygen ions is applied on the two samples depicted in Figs. 10 and 13(c). The material removal is chosen as relatively small, below 10 nm, to avoid inhomogeneous matrix structure effects. The effect of the subsequent oxygen machining on surface roughness of RSA Al905 and RSA Al6061 is summarized in Table 4 and the corresponding ion beam process parameter in Table 2.

The AFM measurements in Fig. 15(b) represent the RSA Al905 initial surface, after two runs IBP, and after a subsequent oxygen process. After RIBE machining with oxygen process gas, the turning marks corresponding to the deviations in the spatial frequency range of 5 to 0.5 μm^{-1} remain almost unchanged [see Fig. 15(a)].

However, their height is slightly increased to (6.6 ± 0.6) nm after the subsequent machining with oxygen process gas. No further etch pit formation can be observed since the etch depth is

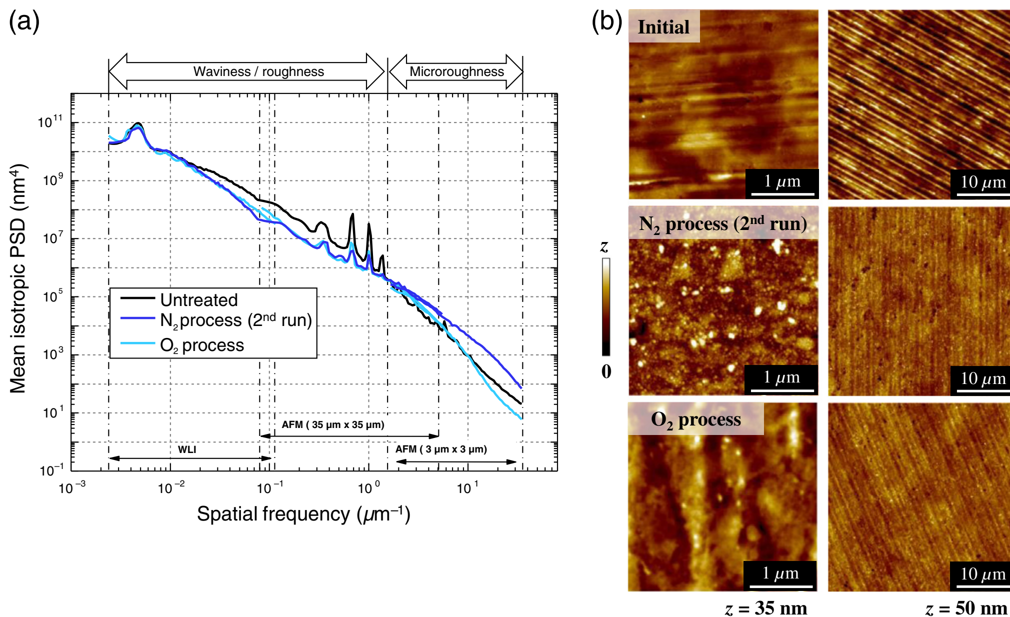

Fig. 15 (a) PSD function of the untreated RSA Al905 surface, after the second planarization run and after the subsequent oxygen process. The PSD functions are calculated on the basis of AFM measurements with scan sizes of 3 $\mu m \times 3$ μm and 35 $\mu m \times 35$ μm and WLI measurements with image sizes of 1230 $\mu m \times 925$ μm and 624 $\mu m \times 467$ μm. (b) AFM measurements (3 $\mu m \times 3$ μm and 35 $\mu m \times 35$ μm) of the untreated RSA Al905 surface (top), after the second planarization run (middle), and after the subsequent oxygen process (bottom).

chosen to be small. Hence, the roughness value is kept constant after oxygen machining. On the contrary, the microroughness is remarkably reduced to a value of 2.2 nm rms. Consequently, the PSD spectrum is decreased in the spatial frequency range above 2 μm^{-1} to a maximum 1.5 dec [see Fig. 15(a)]. Above 10 μm^{-1} spatial frequency, the PSD curve is even below the untreated surface.

The particles observed after two planarization runs are remarkably reduced after oxygen machining. Additionally, the granular structure that occurred after nitrogen machining is removed, resulting in the large decrease in the high-spatial frequency range (see Fig. 15). Consequently, the full range roughness decreases to (5.7 ± 1.1) nm rms.

During subsequent oxygen machining, the material removal of a few nanometer is sufficient for eliminating the granular structure formed after IBP. Therefore, we assume that a modified layer may be formed on the aluminum surface after nitrogen machining. To analyze the effect in detail, the chemical surface modification after IBP and subsequent oxygen machining is analyzed by TOF-SIMS experiments.

A native oxide layer is formed instantly during the contact of pure aluminum surface with air. Since the samples are exposed to air after machining, the existence of a surface oxide layer is expected on all samples. The AlO^- signal is used to illustrate the extent of the surface oxide layer. In addition, the AlN^- signal is used to illustrate the extent of a nitride surface layer after planarization with nitrogen process gas (see Fig. 16).

The oxide and nitride layer thickness is ascertained as the distance of the surface to the depth, where the signal is decreased to its half maximum value. After two planarization runs, a 15.3-nm thick nitride layer is formed on the aluminum surface overlapping with an ~7.9-nm thick oxide layer revealed on the surface. This oxide layer may be due to the formation of a native oxide layer when aluminum is exposed to air after processing. Note that these layers are not independently present on the surface but exist in an oxynitride surface layer with 13.3 nm in thickness.

After subsequent oxygen machining, the depth of the oxide layer is significantly enlarged to 18.5 nm overlapping with a 16.8-nm-thick nitride layer. The oxynitride layer is increased to 15.7 nm. Consequently, an oxidation process of the surface during subsequent RIBE finishing with oxygen operating gas has to be considered.

A similar effect has been observed in direct aluminum machining with oxygen process gas.[13] The oxide layer formed on the aluminum surface after 380 nm machining has a similar depth.

Oxygen machining is also performed on RSA Al6061 after two runs IBP. The AFM measurements in Fig. 17(b) represent the initial surface, after two runs IBP, and after a subsequent oxygen process.

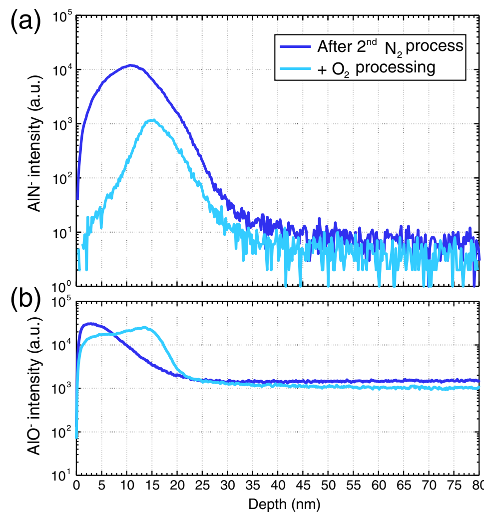

Fig. 16 TOF-SIMS depth profiles of RSA Al905 after two planarization runs using nitrogen process gas and after the subsequent oxygen machining. (a) The extent of a nitride surface layer is represented by the AlN^- signal. (b) The surface oxide layer is represented by the AlO^- signal.

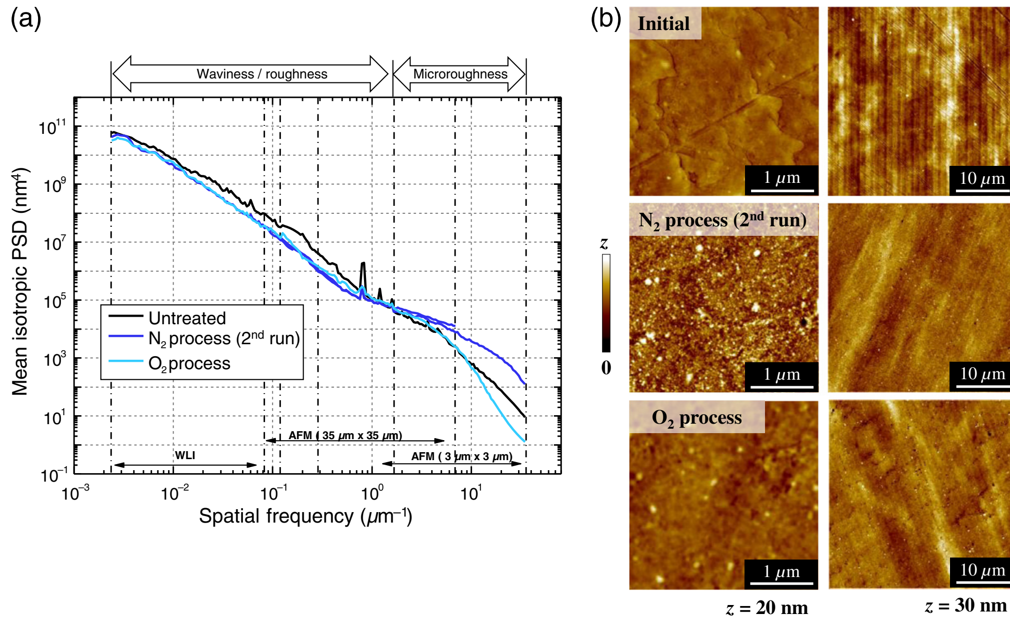

Fig. 17 (a) PSD function of the untreated RSA Al6061 surface, after the second planarization run, and after the subsequent oxygen process. The PSD functions are calculated on the basis of AFM measurements ($3\ \mu m \times 3\ \mu m$ and $35\ \mu m \times 35\ \mu m$) and WLI measurements with image sizes of $1230\ \mu m \times 925\ \mu m$ and $624\ \mu m \times 467\ \mu m$. (b) AFM measurements of RSA Al6061 ($3\ \mu m \times 3\ \mu m$ and $35\ \mu m \times 35\ \mu m$) initial surface (top), after the second planarization run (middle), and after the subsequent oxygen process (bottom).

After RIBE machining with oxygen process gas, the roughness value remains unchanged. By contrast, the formation of etch pits is increased with sizes up to several hundred nanometers [see Fig. 17(b)]. They seem to preferentially order at the grain boundaries of the RSA Al6061 material. This observation is similar to the recently reported work[13] in which a series of ordered etch pits is formed after 400 nm material removal with oxygen process gas. Due to the low machining depth in these experiments, the etch pit formation is comparably sparse.

By contrast, the microroughness is remarkably decreased after the oxygen process to a value of 1.4 nm rms. As a consequence, the PSD spectrum is remarkably decreased in the spatial frequency range above $3\ \mu m^{-1}$ to a maximum 2 dec. Above $10\ \mu m^{-1}$, the PSD curve is even below the initial surface roughness [see Fig. 17(a)]. The granular structure is removed after subsequent oxygen machining, but single particles in the submicrometer range are still apparent after oxygen machining. In summary, the full range roughness decreases to (3.6 ± 0.6) nm rms.

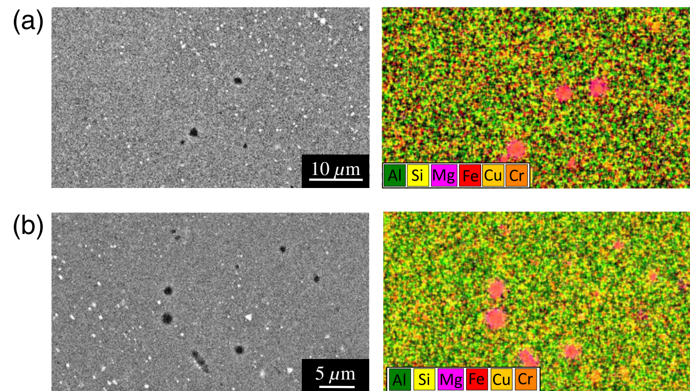

Fig. 18 (a) SEM and SEM-EDX analysis of aluminum RSA Al6061 alloy after two runs of IBP and (b) after subsequent oxygen machining revealing significant Mg and Si precipitations within the etch pits and particle formation due to Si, Cr, and Fe. No distinct difference in local composition distribution was observed before and after RIBE machining with oxygen process gas.

The local composition distribution after oxygen processing is monitored by SEM-EDX mapping (see Fig. 18). As a remarkable result, Mg and Si fractions are found together within the etch pits after IBP and subsequent oxygen processing. The particles formed on the surface are mainly due to Si, Cr, Cu, and Fe. Similar observations are made after direct aluminum machining with nitrogen process gas after 300 nm material removal (see Fig. 9).

The formation of etch pits after nitrogen processing of the sample depicted in Figs. 8 and 13 is comparably low despite the strikingly decreased material removal during oxygen machining. We assume that Mg and Si fractions are preferentially eroded during oxygen machining, resulting in an increased pit formation.

4 Conclusions

Our results on IBP of aluminum surfaces are based upon a two-step process including IBP using nitrogen process gas and direct aluminum machining with oxygen process gas. In particular, we examined a preparation sequence for negative photoresist ma-N 2405 with the aid of a planarization layer to smooth technical aluminum surfaces. The prebaking is necessary to evaporate the majority of organic solvent, and DUV exposure initiates the cross-linking of phenolic resin. Postbaking at 150°C for 6 min on aluminum surfaces and 2 min on thin silicon wafer increases the thermal stability and etch resistance of the photoresist to realize steady-state conditions during IBP. The etch rate is kept constant and the initial smooth surface of the photoresist layer is preserved during machining. Postbaking at temperatures ≥300°C increases the surface roughness due to photoresist degradation caused by thermal decomposition.

During IBP, a highly modified CN_x rich graphitized layer is formed on top of the photoresist with a certain size of microroughness initially introduced after 76 nm material removal. With increasing machining depth, the spatial distribution of the surface roughness changes little. Hence, the smooth surface of the initial photoresist layer is mainly preserved during IBP, and a steady-state etch rate is reached.

PSD analysis shows that the surface roughness of technical aluminum RSA Al905 is decreased in the spatial frequency range of ∼0.03 to 2 μm^{-1} after two planarization runs and the turning mark height is successfully reduced by 82%. The microroughness is increased during the first IBP run and is kept steady-state during the second planarization run. The precipitate structures within the aluminum base material and the formation of a 15.3-nm-thick nitride surface layer may be a key contribution for the increase in microroughness during nitrogen machining. The turning marks of RSA Al6061 are similarly strongly reduced in height to values in the subnanometer range, indicating comparable improvement. The surface roughness is decreased in the spatial frequency range of 0.01 to 1.6 μm^{-1}. The microroughness is increased comparably, showing the same granular like structure after machining.

An improvement of the microroughness of RSA Al905 and RSA Al6061 was found for a subsequent oxygen process. The native oxide layer is enlarged during RIBE machining with oxygen operating gas to about 18 nm thickness. As a consequence of the finishing process, the microroughness is remarkably decreased to 1.4 nm rms of RSA Al6061 and 2.2 nm rms of RSA Al905 surface while preserving the improved waviness and roughness during IBP with N_2 operating gas. RSA Al905 exhibits less etch pit formation than RSA Al6061 during oxygen machining.

In addition to the RIBE-based surface figuring technique that preserves the initial roughness during machining,[13] this promising technology enables the smoothing of high-spatial frequency errors of single-point diamond turned aluminum alloys while preserving or even improving the initial microroughness.

The two-step process was applied on flat surfaces during the present study. However, the process is not limited to flat surfaces but can also be applied to curved surfaces. For IBP investigations, a five-axis motion system was used, which allows the adjusting of the sample to the ion source in a way that the ion beam incidence angle is continuously normal to the sample surface. However, a further optimization of the photoresist application procedure is necessary since the applied spin-coating within the present study might be limited due to the viscosity of the planarizing layer. For the plane transfer, a constant layer thickness over the entire surface is necessary, which could be achieved with a spray-coating process.

Acknowledgments

The authors are very grateful to Mr. T. Liebeskind for chemical sample treatments, Mrs. Reinhardt for TG and DSC measurements, Mrs. N. Schoenherr for IR measurements, and Mr. D. Hirsch for EDX and XPS analysis and SEM imaging. This work was supported by the German Federal Ministry of Education and Research (BMBF) within the framework of the InnoProfile Transfer initiative (No. 03IPT706X) "Ultraprecision manufacturing using atomic particle beams" is gratefully acknowledged.

References

1. F. Delplanckea et al., "Star separator system for the dual-field capability (PRIMA) of the VLTI," *Proc. SPIE* **5491**, 1–8 (2004).
2. G. P. H. Gubbels et al., "Rapidly solidified aluminium for optical applications," *Proc. SPIE* **7018**, 70183A (2008).
3. R. Steinkopf et al., "Metal mirrors with excellent figure and roughness," *Proc. SPIE* **7102**, 71020C (2008).
4. D. Vukobratovich and J. P. Schaefer, "Large stable aluminum optics for aerospace applications," *Proc. SPIE* **8125**, 81250T (2011).
5. J. P. Rozelot, R. Bingham, and D. D. Walker, "Aluminium mirrors versus glass mirrors," in *ESO Conf. Progr. Telesc. and Instrum. Technol. (ed. M.-H. Ulrich, Garching), ESO Conf. and Workshop Proc. No. 42* (1992).
6. J. S. Browder, S. S. Ballard, and P. Klocek, "Physical properties of infrared optical materials," Chapter 4 in *Handbook of Infrared Optical Materials*, P. Klocek Ed., pp. 141–154, CRC Press, Marcel Dekker, Inc, New York (1991).
7. G. P. H. Gubbels, B. W. H. Venrooy, and R. Henselmans, "Accuracy of freeform manufacturing processes," *Proc. SPIE* **7426**, 742607 (2009).
8. S. Risse et al., "Novel TMA telescope based on ultra-precise metal mirrors," *Proc. SPIE* **7010**, 701016 (2008).
9. J. Zhang et al., "Design and manufacture of an off-axis aluminium mirror for visible-light imaging," *Curr. Opt. Photonics* **1**, 364–371 (2017).
10. Y. Li, H. Takino, and F. Frost, "Ion beam planarization of diamond turned surfaces with various roughness profiles," *Opt. Express* **25**(7), 7828 (2017).
11. Y. Li, H. Takino, and F. Frost, "Characteristics of diamond turned NiP smoothed with ion beam planarization technique," *J. Eur. Opt. Soc.-Rapid Publ.* **13**(1), 27 (2017).
12. S. L. Folkman, "Characterization of electroless nickel plating on aluminum mirrors," *Proc. SPIE* **4771**, 254–264 (2002).
13. J. Bauer, F. Frost, and T. Arnold, "Reactive ion beam figuring of optical aluminium surfaces," *J. Phys. D* **50**(8), 85101 (2017).
14. J. Bauer et al., "Finishing of metal optics by ion beam technologies," *Opt. Eng.* **58**(9), 092612 (2019).
15. L. F. Johnson, K. A. Ingersoll, and D. Kahng, "Planarization of patterned surfaces by ion beam erosion," *Appl. Phys. Lett.* **40**, 636–638 (1982).
16. L. F. Johnson and K. A. Ingersoll, "Ion polishing with the aid of a planarizing film," *Appl. Opt.* **22**, 1165–1167 (1983).
17. R. ter Horst et al., "Diamond turning and polishing tests on new RSP aluminium alloys," *Proc. SPIE* **8450**, 84502M (2012).
18. Micro Resist Technology GmbH, "Processing guideline of ma-N 2400 negative photoresist," Berlin, Germany, 2014, https://www.microresist.de (accessed 12 July 2017).
19. Osram, "Technical information data sheet of mercury short arc lamp HBO 350 W/S," 2019, https://www.osram.de (accessed 13 July 2017).
20. J. Bauer et al., "Improved ion beam tools for ultraprecision figure correction of curved aluminum mirror surfaces," *J. Astron. Telesc. Instrum. Syst.* **4**(4), 046003 (2018).
21. G. Gubbels, L. Tegelaers, and R. Senden, "Melt spun aluminium alloys for moulding optics," *Proc. SPIE* **8884**, 88841W (2013).

22. J. F. Jørgensen, "The scanning probe image processor SPIP™, user's and reference guide," Version 4.2, Image Metrology, Denmark, 2018, http://www.imagemet.com/WebHelp6/Default.htm (accessed 22 August 2018).
23. A. Voigt, "Zur Chemie photolytisch generierter Arylnitrene in Polymermatrizen," Humboldt-Universität zu Berlin, Mathematisch-Naturwissenschaftliche Fakultät I (1998).
24. H. Steppan, G. Buhr, and H. Vollmann, "Resisttechnik - ein Beitrag der Chemie zur Elektronik," *Angew. Chem. Int. Ed.* **94**(7), 471–485 (2006).
25. A. Voigt et al., "Nanometer patterning using ma-N 2400 Series DUV negative photoresist and electron beam lithography," *Proc. SPIE* **3676**, 1–7 (1999).
26. H. Elsner et al., "Evaluation of ma-N 2400 Series DUV photoresist for electron beam exposure," *Microelectron. Eng.* **46**, 389–392 (1999).
27. M. Hashimoto et al., "Photochemistry of azide-phenolic resin photoresists," *Polym. Eng. Sci.* **26**, 1090–1095 (1986).
28. M. Hesse, H. Meier, and B. Zeeh, *Spektroskopische Methoden in der organischen Chemie*, 7. Überarbeitete Auflage, pp. 40–67, George Thieme Verlag, Stuttgart, New York (2005).
29. H. Lobo and J. V. Bonilla, *Handbook of Plastics Analysis*, Marcel Dekker, New York (2003).
30. R. Conley and J. Bieron, "A study of the oxidative degradation of phenol-formaldehyde polycondensates using infrared spectroscopy," *J. Appl. Polym. Sci.* **7**(1), 103–117 (1963).
31. J. Huang et al., "Controlled synthesis of high-ortho-substitution phenol-formaldehyde resins," *J. Appl. Polym. Sci.* **97**(2), 652–658 (2005).
32. E. Lieber et al., "Infrared spectra of acid azides, carbamyl azides and other azido derivatives: Anomalous splittings of the N_3 stretching bands," *Spectrochim. Acta.* **19**(7), 1135–1144 (1962).
33. W. M. Jackson and R. T. Conley, "High temperature oxidative degradation of phenol-formaldehyde polycondensates," *J. Appl. Polym. Sci.* **8**, 2163–2193 (1964).
34. R. T. Conley, "Oxidative degradation of phenol-formaldehyde polycondensation initial degradation reactions," *J. Appl. Polym. Sci.* **9**, 1117–1126 (1965).
35. G. P. Shulman and H. W. Lochte, "Thermal degradation of polymers. 2. Mass spectrometric thermal analysis of phenol-formaldehyde polycondensates," *J. Appl. Polym. Sci.* **10**, 619–635 (1965).
36. J. Kim, "Electrochemical studies of carbon films from pyrolyzed photoresist," *J. Electrochem. Soc.* **145**(7), 2314 (1998).
37. M. Sumiya et al., "Study of 193 nm photoresist degradation during short time fluorocarbon plasma exposure. I. Studies of modified layer formation," *J. Vac. Sci. Technol. B* **26**, 1637 (2008).
38. M Sumiya et al., "Study of 193 nm photoresist degradation during short time fluorocarbon plasma exposure. III. Effect of fluorocarbon film and initial surface condition on photoresist degradation," *J. Vac. Sci. Technol. B* **26**, 1978–1986 (2008).
39. B. E. Schuster et al., "Characterization of the morphology and composition of commercial negative resists used for lithographic processes," *Anal. Bioanal. Chem.* **393**(8), 1899–1905 (2009).
40. G. ten Brinke, F. E. Karasz, and T. S. Ellis, "Depression of glass transition temperatures of polymer networks by diluents," *Macromolecules* **16**(2), 244–249 (1983).
41. G. Carter, "The physics and applications of ion beam erosion," *J. Phys. D. Appl. Phys.* **34**, R1–R22 (2001).
42. M. J. Nobes, J. S. Colligon, and G. Carter, "The equilibrium topography of sputtered amorphous solids," *J. Mater. Sci.* **4**, 730–733 (1969).
43. G. Carter, J. S. Colligon, and M. J. Nobes, "The equilibrium topography of sputtered amorphous solids II," *J. Mater. Sci.* **6**, 115–117 (1971).
44. G. Carter, M. J. Nobes, and J. L. Whitton, "The stability of equilibrium surface topography developed by sputtering," *J. Mater. Sci.* **13**, 2725–2728 (1978).
45. F. Frost et al., "Large area smoothing of surfaces by ion bombardment: fundamentals and applications," *J. Phys. Condens. Matter* **21**, 224026 (2009).
46. F. Frost, A. Schindler, and F. Bigl, "Ion beam smoothing of indium-containing III-V compound semiconductors," *Appl. Phys. A* **66**, 663–668 (1998).

Melanie Ulitschka received her bachelor's degree in industrial engineering, specializing in material engineering and plastics technology, and her master's degree in composite materials from Hof University of Applied Sciences. She worked from 2015 to 2017 as a research assistant at the Institute for Materials Science in Hof. Since 2017, she has been a research assistant and doctoral candidate at Leibniz Institute of Surface Engineering (IOM) in Leipzig.

Jens Bauer received his diploma degree in physics and finished his PhD at the Institute of Inorganic Chemistry of the University of Leipzig in 2009. Afterward, he worked in institutional research as well as in several companies with a focus on nanomaterial and thin film technology. Since 2014, he investigates optical device finishing by ion beam technologies at the Leibniz Institute of Surface Engineering, Leipzig. As an author, he has contributed to 27 peer-reviewed papers.

Frank Frost received his doctorate degree from the University of Leipzig in 1998. His research focuses on fundamental investigations of the manufacturing of nano- and microstructures using (reactive) ion beam etching (RIBE), pattern formation due to ion beam driven self-organization, the use of ion beam processes for smoothing and planarization down to sub 0.1 nm surface roughness level, and the implementation of these technologies in production practice. He has authored/co-authored more than 130 papers.

Thomas Arnold has been active in the area of ultraprecision surface machining for more than 20 years. His current research interests include technology development for optical freeform surface fabrication by ion beams as well as chemically reactive plasma jets targeting form accuracy in the nanometer range. He is the author of 30 peer-reviewed papers. Since 2014, he has been an endowed professor for ultraprecision surface machining using ions and plasmas at the Technische Universität Dresden, Germany.